

## Article

# Semi-Spontaneous Post-Crosslinking Triblock Copolymer Electrolyte for Solid-State Lithium Battery

Zhenan Zheng <sup>1,2</sup>, Jie Huang <sup>1</sup>, Xiang Gao <sup>2,\*</sup> and Yingwu Luo <sup>2</sup>

<sup>1</sup> Fujian Provincial Key Laboratory of Modern Analytical Science and Separation Technology, College of Chemistry, Chemical Engineering and Environment, Minnan Normal University, Zhangzhou 363000, China; zhenan@zju.edu.cn (Z.Z.)

<sup>2</sup> State Key Laboratory of Chemical Engineering, College of Chemical and Biological Engineering, Zhejiang University, Hangzhou 310027, China

\* Correspondence: gaox@zju.edu.cn

**Abstract:** The solid polymer electrolyte is a promising candidate for solid-state lithium battery because of favorable interfacial contact, good processability and economic availability. However, its application is limited because of low ionic conductivity and insufficient mechanical strength. In this study, the delicate molecular structural design was realized via controlled / “living” radical polymerization in order to decouple the trade-off between ionic conductivity and mechanical strength. The random and triblock copolymer electrolytes were designed and synthesized to investigate the influence of molecular structure on ionic conduction, while a chemical cross-linking network was constructed via a semi-spontaneous post-crosslinking reaction. Compared with a random counterpart, the triblock copolymer electrolyte presented stronger chain segment motion and a liquid-like mechanical response due to the independent ion-conducting block, resulting in significantly improved ionic conductivity (from  $6.29 \pm 1.11 \times 10^{-5}$  to  $9.57 \pm 2.82 \times 10^{-5}$  S cm<sup>-1</sup> at 60 °C) and cell performance. When assembled with LiFePO<sub>4</sub> and lithium metal electrodes, the cell with triblock copolymer electrolyte showed significantly improved rate performance (150 mAh g<sup>-1</sup> at 1 C) and cycling life (200 cycles with 92.8% capacity retention at 1 C). This study demonstrates the advantages of molecular structure regulation on ionic conduction and mechanical support, which may provide new insights for the future design of solid polymer electrolytes.

**Keywords:** solid polymer electrolyte; molecular structure regulation; semi-spontaneous post-crosslinking reaction



**Citation:** Zheng, Z.; Huang, J.; Gao, X.; Luo, Y. Semi-Spontaneous Post-Crosslinking Triblock Copolymer Electrolyte for Solid-State Lithium Battery. *Batteries* **2023**, *9*, 465. <https://doi.org/10.3390/batteries9090465>

Academic Editor: Ahmad Azmin Mohamad

Received: 25 July 2023

Revised: 2 September 2023

Accepted: 8 September 2023

Published: 13 September 2023



**Copyright:** © 2023 by the authors. Licensee MDPI, Basel, Switzerland. This article is an open access article distributed under the terms and conditions of the Creative Commons Attribution (CC BY) license (<https://creativecommons.org/licenses/by/4.0/>).

## 1. Introduction

Solid-state lithium batteries are one of the most promising next-generation energy storage devices owing to their potential for high energy density and enhanced innate safety [1,2]. As a critical component of solid-state lithium batteries, solid-state electrolytes (SSEs) have aroused widespread research interest [3–6]. The solid polymer electrolyte (SPE) and solid inorganic electrolyte (SIE) are two of the most important series of SSEs. Although the SIE presents high room-temperature ionic conductivity and superior thermal stability, factors such as brittleness, poor contact with electrodes and an unstable electrode/electrolyte interface prevent its practical application. Compared with SIE, SPE demonstrates low interfacial resistance, good process-ability and economic availability, and thus is promising for realizing large-scale industrial production [7].

The challenges faced by SPE are low ionic conductivity, insufficient mechanical strength, and a narrow electrochemical stability window (especially resistance to oxidation at the cathode) [8]. Among these, the trade-off between ionic conductivity and mechanical strength is compelling and overwhelming [9]. Since the transfer of lithium-ions in SPE depends on the movement of polymer chain segments, the methods reported in the literature to improve ionic conductivity can be summarized into three categories. The first

category is to destroy the crystalline region and expand the amorphous region by blending, copolymerization or adding fillers [10–12]; the second category is to select monomers with low glass transition temperature [13–15]; and the third category is the introduction of plasticizers, such as room-temperature ionic liquid, plastic crystals, etc. [16–18]. The above methods enhance ionic conductivity by improving the mobility of the polymer chain segment, but sacrifices the mechanical strength of the polymer electrolyte to varying degrees. The study of Monroe and Newman has shown that increasing the mechanical strength of SPE is beneficial to inhibit the lithium dendrites on the surface of lithium metal, thus avoiding short-circuiting within the battery [19]. Therefore, achieving high ionic conductivity and superior mechanical strength simultaneously is still regarded as a vital challenge.

Crosslinking is valid for enhancing the mechanical strength of SPE. Due to the advantages of physical crosslinking, high glass transition temperature, and microphase separation, polystyrene-*b*-poly (ethylene oxide) (PS-*b*-PEO) block copolymers have been extensively researched [20–22]. However, even with a 3D bi-continuous phase morphology, which is most conducive to the transfer of lithium ions, the measured ion conductivity is significantly lower than the theoretical value [23–25]. Meanwhile, several studies have revealed that increasing the volume fraction of PEO can significantly improve the ionic conductivity of PS-*b*-PEO, because it reduces the proportion of excluded ion-conducting zones at the PS/PEO interface, which are called “dead zones” [26]. However, the mechanical strength of amorphous PEO is too weak to block the growth of lithium dendrites [27–29]. Consequently, as the composition ratio of styrene decreases, the mechanical strength of the SPE is insufficient to avoid internal short circuit.

Compared with a physical crosslinking network, a chemical crosslinking network formed by chemical bonds provides more solid mechanical support. In current research, polyethylene glycol diacrylate (PEGDA) have been widely used as the ion-conducting oligomers to form a chemical cross-linking network [30–33]. The construction methods mainly included thermal polymerization and photo-polymerization, which follow the free radical polymerization mechanism. However, the molecular weight of PEGDA is limited within 200–1000 g mol<sup>-1</sup> in order to avoid crystallization. Due to the stoichiometric ratio between reaction functional groups, the composition of conductive ion units is too low to reduce the proportion of “dead zone”, which is detrimental to ionic conductivity. Moreover, the chemical crosslinking structure formed by conventional free radical polymerization is heterogeneous [34,35]. As a result, the improvement of mechanical strength and ionic conductivity is inadequate.

Herein, we proposed a chemically post-crosslinking solid block copolymer electrolyte to address the aforementioned issues. The 3-(trimethoxysilyl) propyl acrylate (TMSiPA) and poly (ethylene glycol) methyl ether acrylate (PEGMA) were applied as post-crosslinking monomer and ion-conducting monomer, respectively. Since there are three crosslinking sites in TMSiPA, which is beneficial and efficient to form a three-dimensional network, the composition ratio of PEGMA can be significantly increased to reduce the area of “dead zone”. Moreover, the chemical crosslinking reaction condition is facile without additional initiator. In this study, SPEs with two different molecular chain structures (triblock and random) were synthesized via the reversible addition–fragmentation chain transfer (RAFT) polymerization, and their physical and electrochemical properties were investigated in detail. The solid-state lithium batteries of LiFePO<sub>4</sub>//SPE//Li were assembled and the cell performances were systematically investigated.

## 2. Materials and Methods

### 2.1. Materials

Poly (ethylene glycol) methyl ether acrylate (PEGMA, 480 g mol<sup>-1</sup>, Sigma-Aldrich, St. Louis, MO, USA), 3-(trimethoxysilyl) propyl acrylate (TMSiPA, >93%, Aladdin, Atlanta, GA, USA), 4,4'-azobis (4-cyanovaleic acid) (V501, 98%, Aladdin), anhydrous ethanol (AR, ≥99.7%, Sinopharm Chemical Reagent Co., Ltd., Beijing, China), lithium perchlorate (LiClO<sub>4</sub>, 99.9%, Aladdin), LiFePO<sub>4</sub> (Advanced Lithium Electrochemistry Co., Ltd.,

Taoyuan City, Taiwan), conductive carbon black (super P, Alfa Aesar, Haverhill, MA, USA) and polyvinylidene fluoride (HSV900, Arkema, Colombes, France) were used as purchased without further purification. The RAFT agent, 2-[[dodecyl-sulfanyl] carbonothioyl] sulfanyl] propanoic acid (DSCTSPA), was synthesized and purified as described in the literature [36].

### 2.2. Synthesis of Copolymers via RAFT Solution Copolymerization

The theoretical molecular weight of both poly (TMSiPA-co-PEGMA) (random copolymer) and poly [TMSiPA-b-PEGMA-b-(TMSiPA-co-PEGMA)] (triblock copolymer) is  $30,000 \text{ g mol}^{-1}$  with a different molar ratio for TMSiPA. In a typical triblock copolymer with 10 mol% of TMSiPA, the molecular weight of each block is 1000, 25,000 and 4000 (500-co-3500 in specific), respectively. The synthetic procedure of triblock copolymer is described in detail as follows. Firstly, 3.5 g of RAFT and 0.280 g of V501 were dissolved in 10 g of anhydrous ethanol, and 10 g of TMSiPA was added. Then, the above mixed solution was poured into a three-necked flask. After 30 min deoxygenation by a nitrogen purge, the temperature of the water bath was raised to  $70 \text{ }^\circ\text{C}$  to start the reaction for 4.7 h, and the polyTMSiPA solution was obtained. Then, 1.189 g of polyTMSiPA solution was mixed with 0.014 g of V501, 12.5 g of PEGMA and 10 g of anhydrous ethanol. The mixed solution was added into a three-necked flask. After 30 min deoxygenation by a nitrogen purge, the reaction temperature was raised to  $70 \text{ }^\circ\text{C}$  for 6 h to obtain the poly (TMSiPA-b-PEGMA) solution. The flask was then cooled to room temperature, and injected with a mixed solution containing 0.25 g of TMSiPA, 1.75 g of PEGMA and 0.014 g of V501. The mixture was deoxygenated and reacted at  $70 \text{ }^\circ\text{C}$  for 28 h to obtain the poly [TMSiPA-b-PEGMA-b-(TMSiPA-co-PEGMA)] solution. As for the random copolymer, the molecular weight of PEGMA and TMSiPA is 28,500 and 1500, respectively. The synthetic procedure is described in detail as follows. Firstly, 0.175 g of RAFT and 0.0141 g of V501 were dissolved in 15 g of anhydrous ethanol, and then 14.25 g of PEGMA and 0.75 g of TMSiPA were added. After 30 min deoxygenation by a nitrogen purge, the temperature of the water bath was raised to  $70 \text{ }^\circ\text{C}$  to start the reaction for 6 h, and the poly(TMSiPA-co-PEGMA) solution was obtained.

### 2.3. Synthesis of Solid Copolymer Electrolyte via Thermocuring

A certain amount of  $\text{LiClO}_4$  was dissolved in the poly [TMSiPA-b-PEGMA-b-(TMSiPA-co-PEGMA)] or poly (TMSiPA-co-PEGMA) solution according to the molar ratio of Li/EO of 1/8. The prepared transparent solution was poured into a Teflon Petri dish in the air, and the methoxysilyl group (-Si-OCH<sub>3</sub>) was spontaneously hydrolyzed into the silanol group (-Si-OH). Then, the Teflon Petri dish was heated at  $60 \text{ }^\circ\text{C}$  for 48 h in order to remove most of the ethanol solvent and the hydrolysis reaction byproduct methanol. Then, it was transferred into a  $60 \text{ }^\circ\text{C}$  vacuum oven to further volatilize the redundant solvent and water to promote the dehydration condensation reaction between the silanol groups. After 96 h, a cross-linked and cured copolymer electrolyte membrane was obtained, which was abbreviated as TRI-SPE or RAN-SPE in the following discussion.

### 2.4. Characterization of Synthesized Copolymer Electrolyte

**Conversion rate.** The conversion rate can be evaluated by detecting the number of residual double bonds in the synthesized copolymer via 500 MHz  $^1\text{H-NMR}$ . In order to avoid the spontaneous hydrolysis of TMSiPA in the copolymer, the sample was quickly sealed in a nuclear magnetic tube for detection without treatment. The nuclear magnetic reagent was deuterated chloroform ( $\text{CDCl}_3$ ). The test results and analysis are shown in the supporting information (Figures S1 and S2).

**Gel fraction.** A certain amount of polymer was weighed and extracted with anhydrous ethanol in an oil bath at  $90 \text{ }^\circ\text{C}$  for 60 h. The residue was dried completely at  $120 \text{ }^\circ\text{C}$  under vacuum conditions. The gel fraction was calculated according to the mass difference before and after drying.

**Heat stability.** Pyris 1 TGA (Perkin-Elmer) was applied to measure the thermal decomposition temperature of the polymer electrolyte. The test range was set as 30 to 700 °C with a heating rate of 10 °C min<sup>-1</sup>. The heating process was performed in a nitrogen atmosphere.

**Glass transition temperature.** TA Q200 differential scanning calorimeter was applied to measure the glass transition temperature of synthesized copolymer electrolyte. The test temperature range was -80 °C to 100 °C with a heating rate of 10 °C min<sup>-1</sup>.

**Ionic conductivity.** The AC impedance spectroscopy (EIS) technology in Shanghai Chenhua CHI 660E electrochemical workstation was applied to measure the ionic conductivity of synthesized copolymer electrolyte. The cells consisting of two stainless steel blocking electrodes and synthesized copolymer electrolyte were assembled in a glovebox under an argon atmosphere. The test frequency was 10<sup>-2</sup> to 10<sup>5</sup> Hz. In the Nyquist diagram, the intersection of the straight line and the real part axis in the high frequency region is the measured bulk resistance ( $R_e$ ). The calculation formula is as follows:

$$\sigma = \frac{d}{R_e \times S} \quad (1)$$

where  $d$  is the film thickness (measured by spiral micrometer and the average value of five measurements was applied) and  $S$  is the area of the stainless-steel sheet.

**Lithium-ion migration number.** The lithium-ion migration number of polymer electrolyte was determined by the Bruce-Vincent method using constant potential DC polarization technology and AC impedance spectroscopy technology in the Shanghai Chenhua CHI 660E electrochemical workstation. The test temperature was 60 °C. The synthesized copolymer electrolyte was assembled into a lithium symmetrical battery, and a DC polarization voltage ( $\Delta V$ ) of 10 mV was applied to obtain an initial current ( $I_0$ ) and a stable current ( $I_\infty$ ). The bulk impedance ( $R_{bulk}$ ) of the electrolyte and the interface impedance ( $R_{lithium}$ ) between the electrolyte and lithium metal were obtained by the AC impedance spectra before and after polarization. The calculation formula is as follows:

$$t_{Li^+} = \frac{I_\infty R_{bulk}(\infty) [\Delta V - I_0 R_{lithium}(0)]}{I_0 R_{bulk}(0) [\Delta V - I_\infty R_{lithium}(\infty)]} \quad (2)$$

**Electrochemical stability window.** The polymer electrolyte was assembled into a SS//SPE//Li cell (CR2025) for linear sweep voltammetry (LSV). The voltage scanning range was 0–5 V, and the scanning rate was 0.5 mV s<sup>-1</sup>. The LSV was started at a voltage of 0 V instead of at a voltage of open circuit potential. The test temperature was 60 °C.

**Battery performance.** The electrode slurry was prepared according to the mass ratio of 8:1:1 of LiFePO<sub>4</sub>, conductive carbon black and PVDF with N,N-dimethyl pyrrolidone as dispersion medium. The slurry was coated onto an aluminum foil and dried in a vacuum oven at 120 °C for 24 h and then cut into a  $\phi$ 14 mm wafer as cathode. The thickness of the cathode was 100–120  $\mu$ m, with a load of LiFePO<sub>4</sub> approximately 0.5 g cm<sup>-2</sup>. Then, a CR2025 coin-type cell was assembled with lithium metal ( $\phi$  16  $\times$  0.6 mm) and synthesized copolymer electrolyte. The thickness of synthesized copolymer electrolyte is 200–250  $\mu$ m. The cell performances were evaluated by a Neware battery test system at 60 °C.

**Rheological properties.** The rheological properties of synthesized copolymer electrolyte were tested using a HAAKE RS6000 rotary rheometer. The test temperature was set at 60 °C to detect the viscoelasticity of the electrolyte at the battery operation status. The oscillation mode was adopted, and two test methods were used, which were linear viscoelastic region (LVR) scanning and oscillation frequency scanning. In the LVR test, the oscillation frequency was 1 Hz, and the strain scanning range was 0.01 to 1000%. The relationship between strain ( $\delta$ ) and modulus (including storage modulus  $G'$  and loss modulus  $G''$ ) was obtained and the LVR of the electrolyte was judged, as shown in Figure S3. Combining the test result of LVR and the maximum torque that the instrument can

withstand, a strain of 3% was chosen to perform the oscillation frequency scanning. The scanning frequency was 0.01 to 40 Hz.

### 3. Results and Discussion

#### 3.1. Ionic Conductivity

Triblock and random copolymers with a molecular weight of  $30,000 \text{ g mol}^{-1}$  and different molar ratios of TMSiPA/PEGMA were synthesized via RAFT solution polymerization, and then doped with  $\text{LiClO}_4$  to fabricate solid-state polymer electrolytes, which were abbreviate as TRI-SPE and RAN-SPE. The ionic conductivities of synthesized SPEs at  $60^\circ\text{C}$  were measured. As shown in Figure 1, the ionic conductivity of TRI-SPE increases from  $2.67 \pm 0.31 \times 10^{-5} \text{ S cm}^{-1}$  to  $9.57 \pm 2.82 \times 10^{-5} \text{ S cm}^{-1}$  while the TMSiPA molar ratio decreases from 26% to 10%, attributing to the expansion of ion-conducting domains. When the molar ratio of TMSiPA is set as 10%, TRI-SPE exhibits significantly higher ionic conductivity than RAN-SPE ( $6.29 \pm 1.11 \times 10^{-5} \text{ S cm}^{-1}$ ). The molecular structure of TRI-SPE and RAN-SPE is illustrated in Figure 2a. Compared with the random distribution of monomers in RAN-SPE, the post-crosslinking monomers are immobilized at both ends of a polymer chain in TRI-SPE, while the ion-conducting monomers are concentrated in the middle. Since the ion transport in SPE mainly depends on the segment motion of polymer chain, which can be reflected as glass transition temperature ( $T_g$ ), the differential scanning calorimetry (DSC) analysis was applied to elucidate the influence of molecular structure on ionic conductivity. The  $T_g$  of PEGMA homopolymers is  $-71^\circ\text{C}$  (Figure S4). After the introduction of TMSiPA and  $\text{LiClO}_4$ , the  $T_g$ s of TRI-SPE and RAN-SPE increased to  $-38.5^\circ\text{C}$  and  $-30.7^\circ\text{C}$ , respectively, as shown in Figure 2b. The obvious improvement of  $T_g$ s indicates that the formation of a chemical cross-linking network inhibits the ability of segment motion. Meanwhile, the formation of a chemical cross-linking network is verified by the gel fraction test, which was 40.4% for TRI-SPE and 47.7% for RAN-SPE, respectively. The lower  $T_g$  of TRI-SPE manifested a superior ability of chain segment motion compared with RAN-SPE, thus enhancing the ionic conductivity.

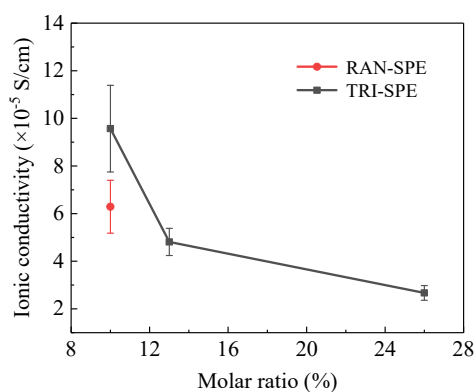


**Figure 1.** The relationship between ionic conductivity (at  $60^\circ\text{C}$ ) and molar ratio of TMSiPA.

Since the ionic conductivity is determined by the concentration of charge carriers and its migration rate, the ionic conductivity of SPE is highly sensitive to temperature variation. The ionic conductivities of TRI-SPE and RAN-SPE were measured every  $10^\circ\text{C}$  at a range of  $30^\circ\text{C}$  to  $100^\circ\text{C}$ . As shown in Figure 3, ionic conductivity increases with rising temperature. There are two reasons for this phenomenon. When the temperature rises, the dissociation degree of lithium salt is improved, thus increasing the concentration of free lithium ions. In addition, the mobility of the polymer chain segment is enhanced, which improves the migration rate of lithium ions. It has been reported that the Arrhenius behavior can be observed when the solvation of lithium ions and polymer matrix happens at a temperature much higher than  $T_g$  [37]. Hence, the data of  $\ln \sigma$  ( $\sigma$  represents ionic conductivity in unit of  $\text{S/cm}$ ) and  $1000/T$  ( $T$  represents test temperature in unit of  $\text{K}$ ) were linearly fitted, as shown

in Figure S5. The goodness of fit ( $R^2$ ) was greater than 98.5%, indicating the relationship between ionic conductivity and temperature conforms to the Arrhenius equation, that is:

$$\sigma = \sigma_0 \exp(-E_a/k_B T), \quad (3)$$

where  $\sigma$  is ionic conductivity,  $\sigma_0$  is the pre-exponential factor,  $E_a$  is the activation energy,  $k_B$  is the Boltzmann's constant, and  $T$  is the absolute temperature. The activation energies of TRI-SPE and RAN-SPE can be calculated from the slope of the fitting line, which are 59.83 and 65.85  $\text{kJ mol}^{-1}$ , respectively. The higher activation energy indicates a larger barrier of lithium-ion transport, and therefore, the trend of activation energy is consistent with ionic conductivity.

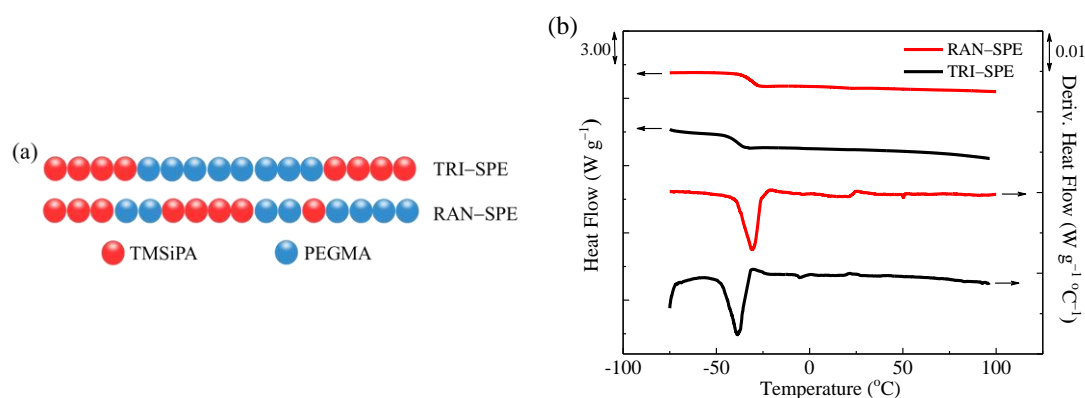


**Figure 2.** (a) Illustration of the molecular structure of TRISPE and RANSPE. (b) DSC curves and corresponding derivative curves of TRI-SPE and RAN-SPE.

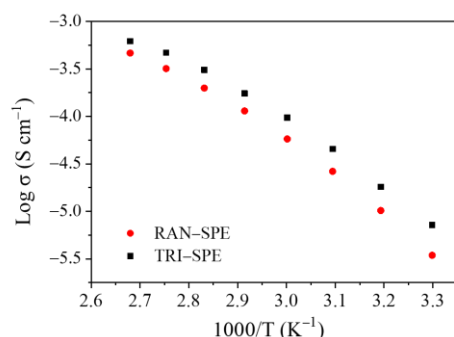


**Figure 3.** Arrhenius plots for SPEs with different molecular structures.

### 3.2. Thermal Stability and Rheological Property

The thermogravimetry analysis curves of PEGMA homopolymer, TMSiPA homopolymer, and synthesized copolymer electrolyte are summarized in Figure 4. The thermal decomposition temperature corresponding to 5% and 50% weight loss and the weight loss fraction at the final thermal decomposition temperature are listed in Table 1. The initial thermal decomposition temperature and final thermal decomposition temperature of TMSiPA homopolymer are highest, while those of PEGMA homopolymer are the lowest. Since the molar ratio of TMSiPA is 10%, the thermal decomposition temperature of TRI-SPE is closer to PEGMA homopolymer. The two transition temperatures in the weight loss curve of TMSiPA homopolymer are related to the cleavage and rearrangement of the Si-O-Si bond to form cyclosiloxane [38]. It can be concluded that the addition of a post-crosslinking monomer, that is TMSiPA, helps improve the thermal stability of the synthesized copolymer electrolyte, which is beneficial in improving the safety of solid-state lithium batteries.

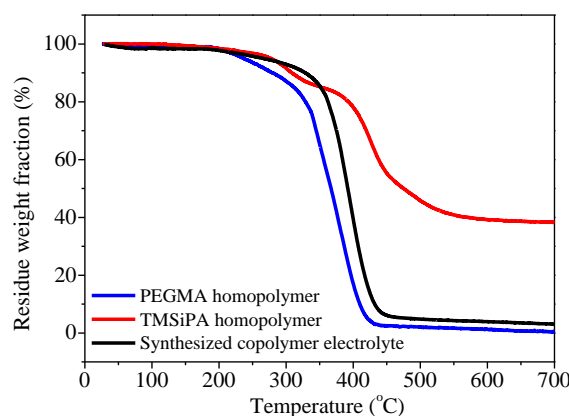
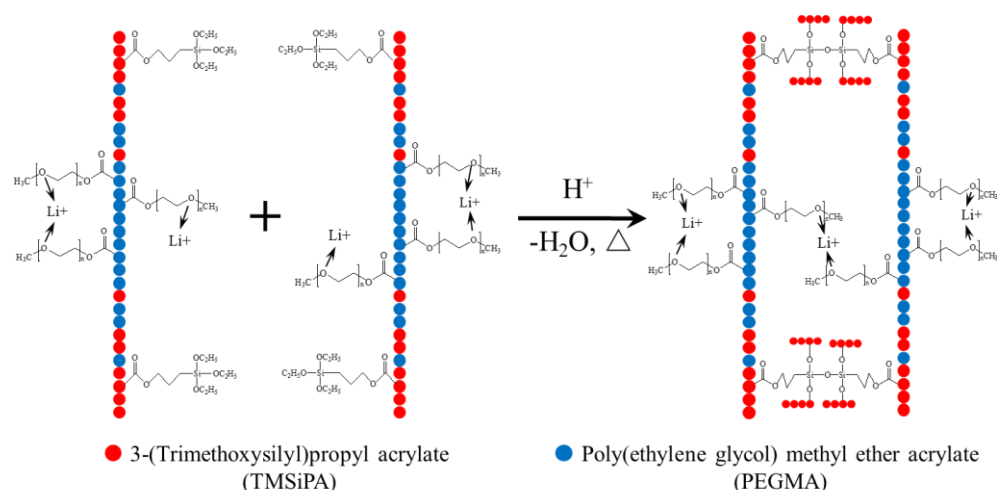


**Figure 4.** Thermogravimetry analysis curves of PEGMA homopolymer, TMSiPA homopolymer and synthesized copolymer electrolyte.

**Table 1.** Weight loss fraction and corresponding thermal decomposition temperature of copolymers.

	5%	50%	Final Weight Loss Fraction and Temperature
PEGMA homopolymer	237 °C	367 °C	97%–434 °C
TMSiPA homopolymer	278 °C	474 °C	60%–588 °C
Synthesized copolymer electrolyte	265 °C	393 °C	95%–492 °C

The post-crosslinking mechanism of TMSiPA is illustrated in Scheme 1. The methoxysilyl group ( $-\text{Si}-\text{OCH}_3$ ) is spontaneously hydrolyzed in air to form silanol group ( $-\text{Si}-\text{OH}$ ), which is subsequently dehydrated to form a  $-\text{Si}-\text{O}-\text{Si}-$  crosslinking network. In addition, each monomer unit has three crosslinking sites, leading to efficient cross-linking network construction. In addition, the delicate molecular structure design in TRI-SPE, as shown in Figure 2a, arranges the cross-linking points at the two ends of a polymer chain, while the soft ion-conducting monomers are in the middle, thus forming an elastic network with good flexibility. The rheological properties of SPEs were evaluated by rotary rheometer at 60 °C to simulate the working state of solid-state battery. As shown in Figure 5a, the complex modulus of SPEs improves as the scanning frequency increases, and the complex modulus of RAN-SPE is much higher than that of TRI-SPE within the test frequency. Since the relaxation time of the chain segment depends on temperature, the variation of frequency is equivalent to the change of observation time at a constant test temperature. When the test frequency is increased, that is, the observation time is shorter, the elastic recovery of the copolymer gradually fails to keep up with the rapid change of the shear force, thus exhibiting viscosity. Meanwhile, the higher complex modulus of RAN-SPE manifests stronger rigidity (that is, poorer chain segment mobility) than TRI-SPE, which is consistent with the trend of glass transition temperature and loss angle tangent ( $\tan \delta$ ). As shown in Figure 5b, the  $\tan \delta$  of SPEs basically remains stable after a brief rise as the test frequency increases. Within the test frequency, the  $\tan \delta$  of RAN-SPE is lower than 1, which means the loss modulus is lower than storage modulus. Therefore, its mechanical response to shear force is closer to solid rather than liquid. On the other hand, the  $\tan \delta$  of TRI-SPE is stable at approximately 1.2 to 1.3 when the test frequency is greater than 10 Hz, showing a mechanical response analogous to liquid. However, the elastic cross-linking network is not damaged because the uncontrolled rise of  $\tan \delta$  is not observed. The liquid-like mechanical response of TRI-SPE leads to better interfacial contact with the electrode by reducing the interface resistance, as demonstrated in the following cell performance tests.



**Scheme 1.** Hydrolysis and dehydration crosslinking mechanism of synthesized copolymer electrolyte.

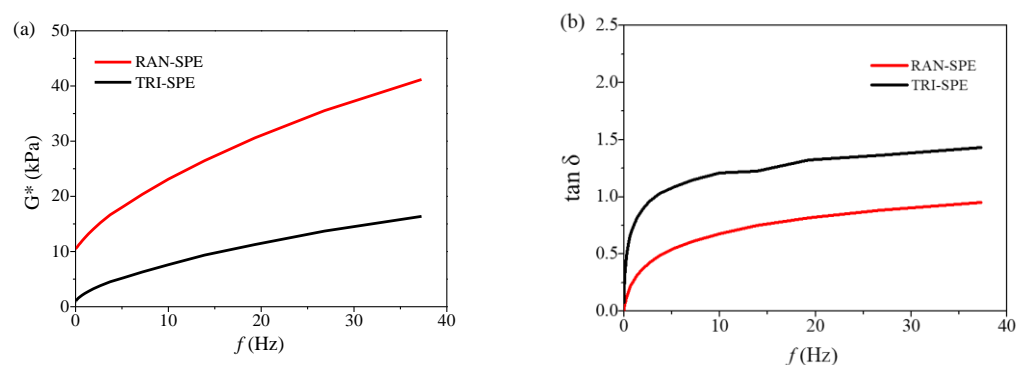


**Figure 5.** Relationship between (a) complex modulus ( $G^*$ ), (b) loss angle tangent ( $\tan \delta$ ) and test frequency of RAN-SPE and TRI-SPE.

### 3.3. Electrochemical Performance

The mass energy density of the battery is equal to the discharge capacity multiplied by the average discharge voltage, so the material with a high discharge voltage platform can improve the energy density of the battery. The application of high-voltage electrodes requires matched electrolytes. Hence, the electrochemical stability window of SPE determines the operating voltage of the battery. The electrochemical stability window is the voltage range in which the electrolyte can work stably without an electrochemical reaction and can be measured by linear sweep voltammetry. The test temperature was set at 60 °C, which is the same as the operating temperature of solid-state lithium batteries in this study. As shown in Figure 6, a small peak appeared at approximately 3.7 V, corresponding to the oxidation of trace residual solvents. When the potential exceeds 4.3 V, the current density appears as an inflection point and begins to increase rapidly, indicating the emergence of oxidative decomposition of the polymer electrolyte. Therefore, the electrochemical stability window of the synthesized copolymer electrolyte is 0–4.3 V.

The conventional electrolyte is composed of binary lithium salt and an additive dissolved in carbonate-based solvent. The electrolyte is absorbed in a polyethylene or polypropylene porous separator to realize the migration of lithium ions between positive and negative electrodes. Although the electrolyte exhibits high ionic conductivity (approximately 1–10 mS/cm) in a wide temperature range, the lithium-ion migration number is generally below 0.5 [39]. This is because the solvation of lithium ions in the electrolyte leads to a large solvation shell, therefore limiting the migration rate of lithium ions [40]. Unlike the lithium ion, the anion can rapidly diffuse in the opposite direction and gradually accumulate on the electrode surface, forming a concentration gradient inside the battery. The concentration overpotential generated by the concentration gradient rises as

the current density increases, which not only limits the charge/discharge rate of the battery, but also reduces the operating voltage of the battery, leading to damage of battery power and energy density. Therefore, a high lithium-ion migration number is beneficial to the improvement of material utilization, power and energy density, which has been manifested in several studies [39,41,42]. The modified Bruce–Vincent method is used to determine the lithium-ion migration number of synthesized copolymer electrolytes by combining DC polarization technology and AC impedance spectroscopy.

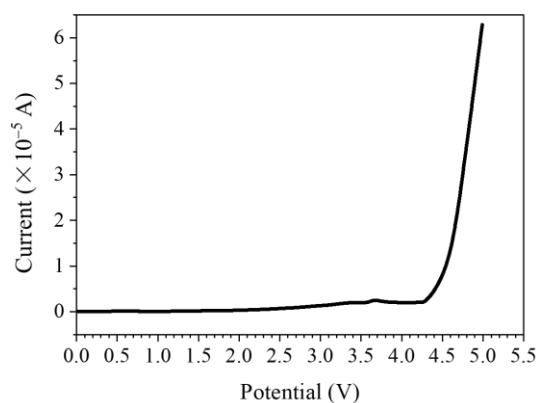


**Figure 6.** Electrochemical stability window of synthesized copolymer electrolyte. The test temperature was 60 °C.

The lithium-ion migration numbers of TRI-SPE and RAN-SPE were calculated to be 0.42 and 0.50, respectively. The test curves are shown in Figures S6 and S7. Under the premise of consistent molecular composition, the influence of molecular structure on the ionic conductivity and lithium-ion migration number is opposite. Compared with RAN-SPE, TRI-SPE has an independent ion-conducting block, and present superior polymer chain segment mobility, as demonstrated by glass transition temperature. The more flexible chain segment mobility is conducive to improving the migration rate of the lithium ion, but also strengthen the solvation of the lithium ion by stronger complexation, which has contradictory effects on the lithium-ion migration number [43]. Therefore, the TRI-SPE present a slightly lower lithium-ion migration number than RAN-SPE.

The synthesized copolymer electrolytes were assembled into  $\text{LiFePO}_4//\text{SPE}/\text{Li}$  half-cells for charge and discharge tests. The rate performances of the half-cells are shown in Figure 7. Obviously, the all-solid-state half-cell fabricated with TRI-SPE presents superior discharge specific capacities than its counterpart at all test rates. When the discharge rate is less than 1 C, the discharge specific capacity is basically maintained at around  $150 \text{ mAh g}^{-1}$  with almost no attenuation. In addition, the discharge specific capacities at 2–5 C discharge rates are 130.5, 94.3, 59.6, and  $42.7 \text{ mAh g}^{-1}$ , respectively. The disparity of discharge specific capacity between all-solid-state half-cells fabricated with RAN-SPE and TRI-SPE gradually increases with the increase of discharge rates. When the discharge rate reaches 2 C, the discharge specific capacity of the TRI-SPE-based cell is approximately threefold higher than that of the RAN-SPE-based cell, that is, 130.5 and  $45.9 \text{ mAh g}^{-1}$ , respectively. When the discharge rate further increases, the discharge specific capacity of the RAN-SPE-based cell is extremely low, and therefore, no data are shown here. Finally, when the discharge rate returned to 0.1 C, the discharge specific capacity basically returned to the initial value with a recovery ratio exceeding 99.5%, indicating that the internal structure of the cell does not suffer irreversible damage. Under the premise of no irreversible damage, the rate performance is dependent on the ionic conductivity and lithium-ion migration number of SPEs. At a higher discharge rate (current density), more electrons pass through the electrode within the same time interval. In the case of a large excess of electrons, the concentration of the lithium ion determines the electrochemical reaction rate, which is reflected as discharge specific capacity. As discussed before, the ionic conductivity of

TRI-SPE is approximately 1.5 times as high as that of RAN-SPE, while the lithium-ion migration number of TRI-SPE is slightly lower than that of RAN-SPE. The synergistic effect of ionic conductivity and lithium-ion migration number makes the half-cell based on TRI-SPE exhibit better rate performance.

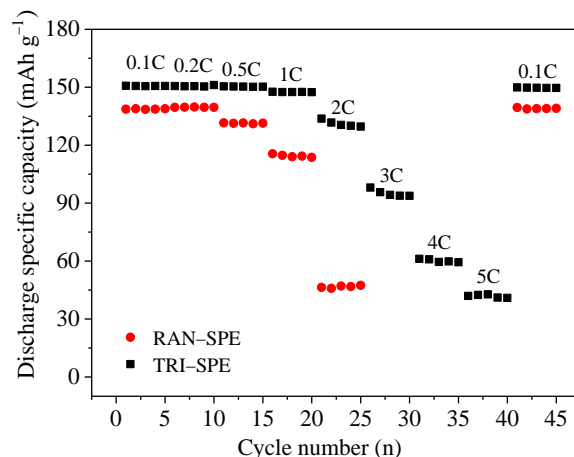


**Figure 7.** Rate performance of  $\text{LiFePO}_4//\text{SPE}/\text{Li}$  half-cells fabricated by synthesized copolymer electrolytes with different molecular structures. The test temperature was  $60\text{ }^\circ\text{C}$ .

The difference in rate performance can be further elucidated by the AC impedance spectrum, which is shown in Figure 8. The solid electrolyte interface impedance ( $R_{\text{SEI}}$ ) in the high frequency region and the charge transfer impedance ( $R_{\text{ct}}$ ) in the intermediate frequency region are fused to form a capacitive reactance arc. The diameter of the arc represents the total impedance value of  $R_{\text{SEI}}$  and  $R_{\text{ct}}$ . The intersection of the left side of the capacitive arc and the real component axis represents the bulk impedance ( $R_{\text{bulk}}$ ) of the half-cell. It can be seen that the  $R_{\text{bulk}}$  and total impedance of TRI-SPE based half-cell are less than that of RAN-SPE. In order to further understand and analyze the impedance response, an equivalent circuit which includes several elements corresponding to each step of the overall battery reaction was built, as shown in Figure S8a. The fitting results are shown in Figure S8b,c. The impedance of  $\text{LiFePO}_4//\text{SPE}/\text{Li}$  half-cell is mainly composed of the following five parts: lithium-ion transfer in synthesized copolymer electrolyte, lithium-ion diffusion in solid electrolyte interface (SEI), lithium-ion transfer at the electrode/electrolyte interface, lithium-ion diffusion in porous electrode, and charge transfer at the interface between electrode and current collector [44,45]. Therefore, in the equivalent circuit,  $R_{\Omega}$  represents the ohmic resistance of electrolyte, current collector and electrode particles,  $R_{\text{SEI}}$  represents the resistance of the solid electrolyte interface,  $R_{\text{ct}}$  represents the resistance of charge transfer and  $W_{\text{o}}$  represents Warburg impedance corresponding to diffusion. Moreover, the measured curve in the Nyquist plot generally deviates from the semicircle, appearing as an arc above the real axis, which is called the capacitive reactance arc. This phenomenon is known as the “dispersion effect”, reflecting that the electric double layer at the electrode interface deviates from the ideal capacitance [45]. As a result, in order to better fit the irregular semicircle, the constant phase element (CPE) is used instead of the capacitor in the equivalent circuit. As discussed above, the impedance value reflects the difficulty of lithium-ion transfer, and then directly affects the rate performance. Additionally, the impedance difference between TRI-SPE and RAN-SPE-based half-cells can be attributed to the different interfacial contacts between the electrode and the electrolyte. In the rheological property test, the mechanical response of TRI-SPE to the external shear force is more similar to liquid, while that of RAN-SPE is closer to solid. Therefore, the interfacial contact between the electrode and the electrolyte is more intimate in a TRI-SPE-based half-cell than that of RAN-SPE, presenting a lower impedance.

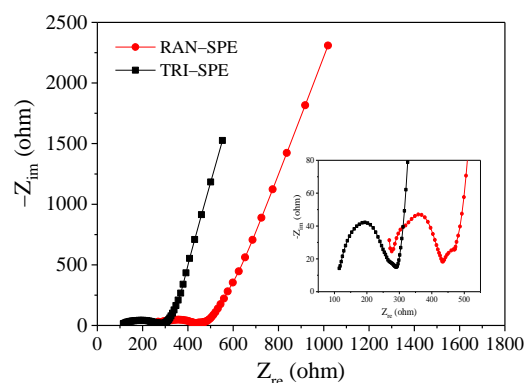


**Figure 8.** Nyquist plots of  $\text{LiFePO}_4//\text{SPE}//\text{Li}$  half-cells fabricated by different synthesized copolymer electrolytes after rate performance tests and at discharge state (inset zoom-in the range of 50–550  $\Omega$ ). The test temperature was 60  $^\circ\text{C}$ .

The cycle life of synthesized copolymer electrolytes was further tested, and the results are shown in Figure 9. At a test rate of 0.2 C, the discharge specific capacity of the RAN-based half-cell decreases from 145.6 to 127.7  $\text{mAh g}^{-1}$  after 180 cycles, with a capacity retention ratio of 87.7%. As for the TRI counterpart, the discharge specific capacity decreases from 152.1 to 145.2  $\text{mAh g}^{-1}$ , with a capacity retention ratio of 95.5%. The Coulombic efficiencies for both half-cells are higher than 99.5% among testing. The test rate was further increased to 1 C to examine the cycle performance of TRI-SPE at a high rate, and the results are shown in Figure 10a. The discharge specific capacity declined from 150.9 to 140.0  $\text{mAh g}^{-1}$  after 200 cycles. The average capacity decay ratio is 0.036% per cycle, which equals to a capacity retention ratio of 92.8%, and the Coulombic efficiency is maintained above 99.5%. The charge and discharge voltage profiles of the first cycle, the 100th cycle and the last cycle are shown in Figure 10b. During the cycle test, the discharge voltage platform of the half-cell reduces continuously, and therefore the polarization voltage between the charge and discharge voltage platforms increases from 0.29 V to 0.46 V. The AC impedance spectrum were conducted at different cycles during the high-rate cycling test, as shown in Figure 10c. As the number of cycles increases, the diameter of the semicircle representing the total impedance of  $R_{\text{SEI}}$  and  $R_{\text{ct}}$  increases significantly.  $R_{\text{SEI}}$  represents the resistance of lithium-ion transfer through the solid electrolyte interface (SEI) between the electrode and electrolyte, and  $R_{\text{ct}}$  represents the charge transfer impedance at the junction of electrons and lithium ions. The larger impedance increases the difficulty of lithium-ion diffusion from the electrolyte to the electrode surface, and reduces the rate of electron binding, which impedes the efficient electrochemical reaction and ultimately reduces the discharge specific capacity.

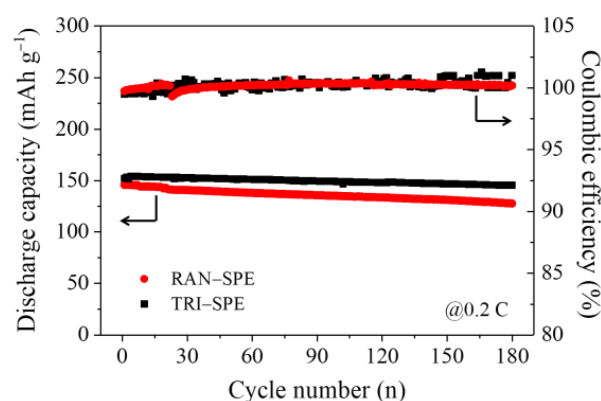


**Figure 9.** Cycle performances and corresponding Coulombic efficiencies of  $\text{LiFePO}_4//\text{SPE}//\text{Li}$  half-cells fabricated by synthesized copolymer electrolytes. The test temperature was 60  $^\circ\text{C}$ .

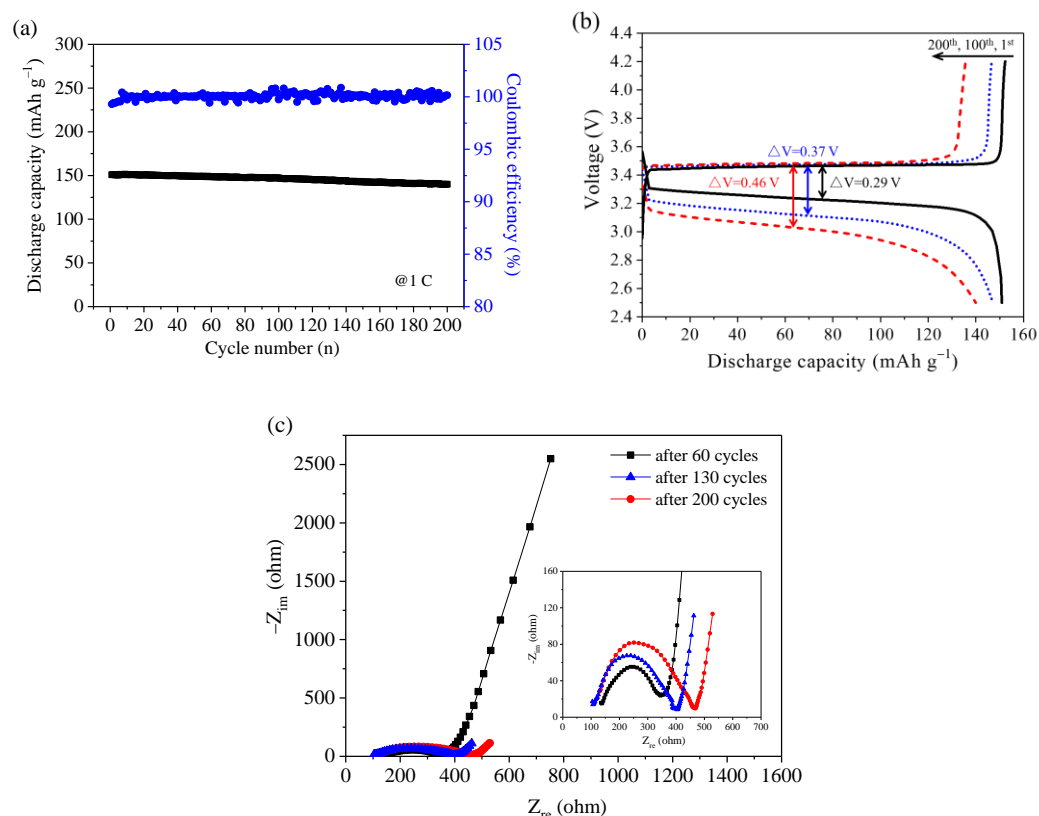


**Figure 10.** (a) Cycle performance and corresponding Coulombic efficiencies of LiFePO<sub>4</sub>//SPE//Li half-cell fabricated by TRI-SPE. (b) Charge and discharge voltage profiles at different cycles. (c) Nyquist plots at different cycles and at discharge state (inset zoom-in the range of 0–700 Ω).

#### 4. Conclusions

In this study, all-solid-state copolymer electrolytes were designed and synthesized via RAFT solution polymerization to regulate the molecular structure. Compared with the commercially common random molecular structure, the advantages of the triblock molecular structure were demonstrated through ionic conductivity, mechanical support, and LiFePO<sub>4</sub> half-cell performance. Due to the independent ion-conducting block, the segmental motion of triblock copolymer is stronger than its random counterpart, resulting in rapid ionic conduction and better cell performance. At the same time, the mechanical properties can be retained by chemical crosslinking reactions. Moreover, the cross-linking points are concentrated at the two ends of the triblock copolymers, leading to a liquid-like mechanical response while maintaining the integrity of the crosslinking network, and thus presenting more intimate contact between the electrode and the electrolyte. The discharge specific capacity of the LiFePO<sub>4</sub> half-cell fabricated by the triblock copolymer electrolyte is higher than 150 mA h g<sup>-1</sup> and shows almost no attenuation until the test rate reaches 2 C. The long-term cycle test also presents a discharge specific capacity of 140.0 mA h g<sup>-1</sup> with high Coulombic efficiency after 200 cycles at a test rate of 1 C. The superior performance of the synthesized triblock copolymer electrolyte proves the advantages of molecular structure regulation on ionic conduction and mechanical support, and may provide new insights for the future design of solid polymer electrolytes.

**Supplementary Materials:** The following supporting information can be downloaded at: <https://www.mdpi.com/article/10.3390/batteries9090465/s1>, Figure S1:  $^1\text{H-NMR}$  spectrum and molecular structural formula (inset) of (a) poly (ethylene glycol) methyl ether acrylate (PEGMA) and (b) 3-(trimethoxysilyl) propyl acrylate (TMSiPA); Figure S2:  $^1\text{H-NMR}$  spectra of (a) poly (PEGMA-co-TMSiPA) random copolymer, (b) poly TMSiPA, (c) poly (TMSiPA-b-PEGMA), and (d) poly [TMSiPA-b-PEGMA-b-(TMSiPA-co-PEGMA)]; Figure S3: Linear viscoelastic region scanning of synthesized copolymer electrolyte; Figure S4: The DSC curve of PEGMA homopolymer; Figure S5: The linear fitting curves of  $\ln \sigma$  and  $1000/T$ ; Figure S6: (a) Time dependence response of DC polarization (10 mV) for Li//RAN-SPE//Li symmetric cell at 60 °C. (b) Impedance spectra of Li//RAN-SPE//Li symmetric cell before and after DC polarization; Figure S7: (a) Time dependence response of dc polarization (10 mV) for Li//TRI-SPE//Li symmetric cell at 60 °C. (b) Impedance spectra of Li//TRI-SPE//Li symmetric cell before and after DC polarization; Figure S8: (a) Equivalent circuit used in this study and (b, c) data fitting results for Figure 8.

**Author Contributions:** Conceptualization, Z.Z. and X.G.; methodology, Z.Z.; validation, Z.Z. and J.H.; investigation, Z.Z. and J.H.; writing—original draft preparation, Z.Z. and J.H.; writing—review and editing, Z.Z., X.G. and Y.L.; visualization, Z.Z.; supervision, X.G. and Y.L.; project administration, X.G. and Y.L.; funding acquisition, X.G., Z.Z. and J.H. All authors have read and agreed to the published version of the manuscript.

**Funding:** This research was funded by the National Natural Science Foundation of China (grant number 21875213) and the Fujian Provincial Natural Science Foundation (grant number 2022J05172 and 2020J01805).

**Data Availability Statement:** Not applicable.

**Acknowledgments:** Thanks to Advanced Lithium Electrochemistry Co., Ltd. for the free supply of  $\text{LiFePO}_4$  samples.

**Conflicts of Interest:** The authors declare no conflict of interest.

## References

1. Manthiram, A.; Yu, X.; Wang, S. Lithium battery chemistries enabled by solid-state electrolytes. *Nat. Rev. Mater.* **2017**, *2*, 16103. [[CrossRef](#)]
2. Lou, S.; Zhang, F.; Fu, C.; Chen, M.; Ma, Y.; Yin, G.; Wang, J. Interface issues and challenges in all-solid-state batteries: Lithium, sodium, and beyond. *Adv. Mater.* **2021**, *33*, 2000721. [[CrossRef](#)] [[PubMed](#)]
3. Zhao, Q.; Stalin, S.; Zhao, C.; Zhao, C.; Archer, L.A. Designing solid-state electrolytes for safe, energy-dense batteries. *Nat. Rev. Mater.* **2020**, *5*, 229–252. [[CrossRef](#)]
4. Chen, J.; Wu, J.; Wang, X.; Zhou, A.; Yang, Z. Research progress and application prospect of solid-state electrolytes in commercial lithium-ion power batteries. *Energy Storage Mater.* **2021**, *35*, 70–87. [[CrossRef](#)]
5. Liu, W.; Yi, C.; Li, L.; Liu, S.; Gui, Q.; Ba, D.; Li, Y.; Peng, D.; Liu, J. Designing polymer-in-salt electrolyte and fully infiltrated 3D electrode for integrated solid-state lithium batteries. *Angew. Chem. Int. Ed.* **2021**, *60*, 12931–12940. [[CrossRef](#)]
6. Famprikis, T.; Canepa, P.; Dawson, J.A.; Islam, M.S.; Masquelier, C. Fundamentals of inorganic solid-state electrolytes for batteries. *Nature Mater.* **2019**, *18*, 1278–1291. [[CrossRef](#)]
7. Cui, G. *Polymer Key Materials of Power Lithium Batteries*, 1st ed.; China Science Publishing & Media Ltd.: Beijing, China, 2018; pp. 80–82. ISBN 978-7-03-058029-0.
8. Li, Z.; Fu, J.; Zhou, X.; Gui, S.; Wei, L.; Yang, H.; Li, H.; Guo, X. Ionic conduction in polymer-based solid electrolytes. *Adv. Sci.* **2023**, *10*, 2201718. [[CrossRef](#)]
9. Zhou, Q.; Ma, J.; Dong, S.; Li, X.; Cui, G. Intermolecular chemistry in solid polymer electrolytes for high-energy-density lithium batteries. *Adv. Mater.* **2019**, *31*, 1902029. [[CrossRef](#)]
10. Wan, J.; Xie, J.; Kong, X.; Liu, Z.; Liu, K.; Shi, F.; Pei, A.; Chen, H.; Chen, W.; Chen, J.; et al. Ultrathin, flexible, solid polymer composite electrolyte enabled with aligned nanoporous host for lithium batteries. *Nat. Nanotechnol.* **2019**, *14*, 705–711. [[CrossRef](#)]
11. Cao, C.; Li, Y.; Feng, Y.; Peng, C.; Li, Z.; Feng, W. A solid-state single-ion polymer electrolyte with ultrahigh ionic conductivity for dendrite-free lithium metal batteries. *Energy Storage Mater.* **2019**, *19*, 401–407. [[CrossRef](#)]
12. Shi, C.; Hamann, T.; Takeuchi, S.; Alexander, G.V.; Nolan, A.M.; Limpert, M.; Fu, Z.; Neill, J.O.; Godbey, G.; Dura, J.A.; et al. 3D asymmetric bilayer carbon-hybridized high-energy-density lithium–sulfur batteries. *ACS Appl. Mater. Interfaces* **2023**, *15*, 751–760. [[CrossRef](#)] [[PubMed](#)]
13. Wang, Q.; Liu, X.; Cui, Z.; Shanguan, X.; Zhang, H.; Zhang, J.; Tang, K.; Li, L.; Zhou, X.; Cui, G. A fluorinated polycarbonate based all solid state polymer electrolyte for lithium metal batteries. *Electrochim. Acta* **2020**, *337*, 135843. [[CrossRef](#)]
14. Zhang, J.; Yang, J.; Dong, T.; Zhang, M.; Chai, J.; Dong, S.; Wu, T.; Zhou, X.; Cui, G. Aliphatic polycarbonate-based solid-state polymer electrolytes for advanced lithium batteries: Advances and perspective. *Small* **2018**, *14*, 1800821. [[CrossRef](#)] [[PubMed](#)]

15. Eriksson, T.; Gudla, H.; Manabe, Y.; Yoneda, T.; Friesen, D.; Zhang, C.; Inokuma, Y.; Brandell, D.; Mindemark, J. Carbonyl-containing solid polymer electrolyte host materials: Conduction and coordination in polyketone, polyester, and polycarbonate systems. *Macromolecules* **2022**, *55*, 10940–10949. [[CrossRef](#)] [[PubMed](#)]
16. Correia, D.M.; Fernandes, L.C.; Martins, P.M.; Garcia, A.C.; Costa, C.M.; Reguera, J.; Lanceros, M.S. Ionic liquid-polymer composites: A new platform for multifunctional applications. *Adv. Funct. Mater.* **2020**, *30*, 1909736. [[CrossRef](#)]
17. Yang, G.; Song, Y.; Wang, Q.; Zhang, L.; Deng, L. Review of ionic liquids containing, polymer/inorganic hybrid electrolytes for lithium metal batteries. *Mater. Des.* **2020**, *190*, 108563. [[CrossRef](#)]
18. Liu, Y.; Zhao, Y.; Lu, W.; Sun, L.; Lin, L.; Zheng, M.; Sun, X.; Xie, H. PEO based polymer in plastic crystal electrolytes for room temperature high-voltage lithium metal batteries. *Nano Energy* **2021**, *88*, 106205. [[CrossRef](#)]
19. Monroe, C.; Newman, J. The Impact of elastic deformation on deposition kinetics at lithium/polymer interfaces. *J. Electrochem. Soc.* **2005**, *152*, A396. [[CrossRef](#)]
20. Young, W.; Kuan, W.; Epps, I.T.H. Block copolymer electrolytes for rechargeable lithium batteries. *J. Polym. Sci. Part B Polym. Phys.* **2014**, *52*, 1–16. [[CrossRef](#)]
21. Sharon, D.; Bennington, P.; Dolejsi, M.; Webb, M.A.; Dong, B.X.; de Pablo, J.J.; Nealey, P.F.; Patel, S.N. Intrinsic ion transport properties of block copolymer electrolytes. *ACS Nano* **2020**, *14*, 8902–8914. [[CrossRef](#)]
22. Grundy, L.S.; Galluzzo, M.D.; Loo, W.S.; Fong, A.Y.; Balsara, N.P.; Takacs, C.J. Inaccessible polarization-induced phase transitions in a block copolymer electrolyte: An unconventional mechanism for the limiting current. *Macromolecules* **2022**, *55*, 7637–7649. [[CrossRef](#)]
23. Villaluenga, I.; Chen, X.C.; Devaux, D.; Hallinan, D.T.; Balsara, N.P. Nanoparticle-driven assembly of highly conducting hybrid block copolymer electrolytes. *Macromolecules* **2015**, *48*, 358–364. [[CrossRef](#)]
24. Wanakule, N.S.; Panday, A.; Mullin, S.A.; Gann, E.; Hexemer, A.; Balsara, N.P. Ionic conductivity of block copolymer electrolytes in the vicinity of order-disorder and order-order transitions. *Macromolecules* **2009**, *42*, 5642–5651. [[CrossRef](#)]
25. Chintapalli, M.; Chen, X.C.; Thelen, J.L.; Teran, A.A.; Wang, X.; Garetz, B.A.; Balsara, N.P. Effect of grain size on the ionic conductivity of a block copolymer electrolyte. *Macromolecules* **2014**, *47*, 5424–5431. [[CrossRef](#)]
26. Bouchet, R.; Phan, T.N.T.; Beaudoin, E.; Devaux, D.; Davidson, P.; Bertin, D.; Denoyel, R. Charge transport in nanostructured PS-PEO-PS triblock copolymer electrolytes. *Macromolecules* **2014**, *47*, 2659–2665. [[CrossRef](#)]
27. Guo, B.; Fu, Y.; Wang, J.; Gong, Y.; Zhao, Y.; Yang, K.; Zhou, S.; Liu, L.; Yang, S.; Liu, X.; et al. Strategies and characterization methods for achieving high performance PEO-based solid-state lithium-ion batteries. *Chem. Commun.* **2022**, *58*, 8182–8193. [[CrossRef](#)]
28. Ge, M.; Zhou, X.; Qin, Y.; Liu, Y.; Zhou, J.; Wang, X.; Guo, B. A composite PEO electrolyte with amide-based polymer matrix for suppressing lithium dendrite growth in all-solid-state lithium battery. *Chin. Chem. Lett.* **2022**, *33*, 3894–3898. [[CrossRef](#)]
29. Fang, R.; Xu, B.; Grundish, N.S.; Xia, Y.; Li, Y.; Lu, C.; Liu, Y.; Wu, N.; Goodenough, J.B. Li<sub>2</sub>S<sub>6</sub>-integrated PEO-based polymer electrolytes for all-solid-state lithium-metal batteries. *Angew. Chem. Int. Ed.* **2021**, *60*, 17701–17706. [[CrossRef](#)]
30. Lee, M.J.; Han, J.; Lee, K.; Lee, Y.J.; Kim, B.G.; Jung, K.N.; Kim, B.J.; Lee, S.W. Elastomeric electrolytes for high-energy solid-state lithium batteries. *Nature* **2022**, *601*, 217–222. [[CrossRef](#)]
31. Wei, Z.; Chen, S.; Wang, J.; Wang, Z.; Zhang, Z.; Yao, X.; Deng, Y.; Xu, X. A large-size, bipolar-stacked and high-safety solid-state lithium battery with integrated electrolyte and cathode. *J. Power Sources* **2018**, *394*, 57–66. [[CrossRef](#)]
32. Piedrahita, C.; Kusuma, V.; Nulwala, H.B.; Kyu, T. Highly conductive, flexible polymer electrolyte membrane based on poly(ethylene glycol) diacrylate-co-thiosiloxane network. *Solid State Ion.* **2018**, *322*, 61–68. [[CrossRef](#)]
33. Hoffmann, M.; Butzelaar, A.J.; Iacob, C.; Theato, P.; Wilhelm, M. Ionogels as polymer electrolytes for lithium–metal batteries: Comparison of poly(ethylene glycol) diacrylate and an imidazolium-based ionic liquid crosslinker. *ACS Appl. Polym. Mater.* **2022**, *4*, 2794–2805. [[CrossRef](#)]
34. Gao, Y.; Zhou, D.; Zhao, T.; Wei, X.; McMahan, S.; Keeffe Ahern, J.O.; Wang, W.; Greiser, U.; Rodriguez, B.J.; Wang, W. Intramolecular cyclization dominating homopolymerization of multivinyl monomers toward single-chain cyclized/knotted polymeric nanoparticles. *Macromolecules* **2015**, *48*, 6882–6889. [[CrossRef](#)]
35. Zhang, M.; Liu, L.; Chang, W.; Li, J. Controllable and reversible dimple-shaped aggregates induced by macrocyclic recognition effect. *Langmuir* **2015**, *31*, 13581–13589. [[CrossRef](#)]
36. Ferguson, C.J.; Hughes, R.J.; Nguyen, D.; Pham, B.T.T.; Gilbert, R.G.; Serelis, A.K.; Such, C.H.; Hawket, B.S. Ab initio emulsion polymerization by RAFT-controlled self-assembly. *Macromolecules* **2005**, *38*, 2191–2204. [[CrossRef](#)]
37. Hallinan, D.T.; Balsara, N.P. Polymer electrolytes. *Annu. Rev. Mater. Res.* **2013**, *43*, 503–525. [[CrossRef](#)]
38. Zhou, W.; Yang, H.; Guo, X.; Lu, J. Thermal degradation behaviors of some branched and linear polysiloxanes. *Polym. Degrad. Stab.* **2006**, *91*, 1471–1475. [[CrossRef](#)]
39. Zhao, Y.; Wang, L.; Zhou, Y.; Liang, Z.; Tavajohi, N.; Li, B.; Li, T. Solid polymer electrolytes with high conductivity and transference number of Li ions for Li-based rechargeable batteries. *Adv. Sci.* **2021**, *8*, 2003675. [[CrossRef](#)]
40. Ue, M. Mobility and ionic association of lithium and quaternary ammonium salts in propylene carbonate and  $\gamma$ -butyrolactone. *J. Electrochem. Soc.* **1994**, *141*, 3336. [[CrossRef](#)]
41. Diederichsen, K.M.; McShane, E.J.; McCloskey, B.D. Promising routes to a high Li<sup>+</sup> transference number electrolyte for lithium ion batteries. *ACS Energy Lett.* **2017**, *2*, 2563–2575. [[CrossRef](#)]

42. Kim, D.; Liu, X.; Yu, B.; Mateti, S.; O'Dell, L.A.; Rong, Q.; Chen, Y.L. Amine-functionalized boron nitride nanosheets: A new functional additive for robust, flexible ion gel electrolyte with high lithium-ion transference number. *Adv. Funct. Mater.* **2020**, *30*, 1910813. [[CrossRef](#)]
43. Mindemark, J.; Lacey, M.J.; Bowden, T.; Brandell, D. Beyond PEO-Alternative host materials for Li<sup>+</sup>-conducting solid polymer electrolytes. *Prog. Polym. Sci.* **2018**, *81*, 114–143. [[CrossRef](#)]
44. Bard, A.J.; Faulkner, L.R. *Electrochemical Methods Fundamentals and Applications*, 2nd ed.; John Wiley & Sons, Inc.: New York, NY, USA, 2001; ISBN 0-471-04372-9.
45. Cao, C.N.; Zhang, J.Q. *An Introduction to Electrochemical Impedance Spectroscopy*, 1st ed.; China Science Publishing & Media Ltd.: Beijing, China, 2002; ISBN 7-03-009854-4.

**Disclaimer/Publisher's Note:** The statements, opinions and data contained in all publications are solely those of the individual author(s) and contributor(s) and not of MDPI and/or the editor(s). MDPI and/or the editor(s) disclaim responsibility for any injury to people or property resulting from any ideas, methods, instructions or products referred to in the content.